TECHNICAL REPORT

High-resolution cross- and sub-fault comparisons of CFM, seismicity, and structural fabric imaged with receiver functions

Principal Investigators: Deborah Kilb (UCSD - Scripps Institution of Oceanography) and Vera Schulte-Pelkum (University of Colorado Boulder)

Here, we report results for fault-crossing arrays in three locations: The San Andreas Fault near Parkfield; the San Jacinto Fault zone in the vicinity of the trifurcation; the Mojave crossing the Ludlow fault and two other minor faults.

Data This work relies on three primary data sets. (1) 3-D CFM 5.3 fault geometry (Hearn et al., 2020; Hughes et al., 2020). (2) 3-D tectonic grain as imaged by receiver functions (RF) (Schulte-Pelkum et al., 2020); and (3) 3-D Seismicity: 1981-2017 SCSN catalog (Hauksson et al., 2012), including locations from the GrowClust algorithm (Trugman and Shearer, 2017), supplemented by a denser 10-year template catalog (Ross et al., 2019).
Method We compare seismicity, anisotropy contrasts imaged with receiver functions (Schulte-Pelkum and Mahan, 2014; Schulte-Pelkum et al., 2020), and CFM fault traces.

San Andreas fault near Parkfield

In our proposal, we showed preliminary results obtained from a subset of stations of the PASO deployment (Thurber et al., 2003, 2004). In this funding cycle, we added data from the PASO reoccupation deployment as well as Plate Boundary Observatory stations (PB), which densified our results significantly (Fig. 1). We make the following observations: 1) Receiver function-imaged strikes (Fig. 1, red bars) align fairly closely to the strike of the San Andreas fault (black lines). 2) Depths of receiver function-imaged fabric contrasts are similar to seismicity depth near the surface fault trace, while deeper contrasts are observed away from the surface fault trace on both sides of the fault. 3) Interestingly, the dip inferred from the phase of the receiver function A1 arrivals (shown as a black tickmark at each station) is asymmetric across the fault and points to the northeast on both sides of the fault with only a few exceptions. 4) A1 conversion amplitudes are larger on the northeast side of the fault. Larger A1 amplitudes may imply a larger fabric contrast, an intermediate to steep foliation dip (rather than a shallow or near vertical foliation dip; Brownlee et al., 2017), or both.

In cross-section (Fig. 2), seismicity outlines a near vertical present-day fault while the larger A1 arrivals trace a structure deepening to the northeast on the northeastern side of the fault, and the fabric is weaker but still dips to the northeast on the southwestern side of the fault. This

relationship allows for an interpretation where strike-slip motion on a nascent San Andreas fault was initially accommodated on northeast-dipping fabric inherited from Farallon subduction (as represented by the smaller amplitude conversions on the southwestern side of the fault) and progressively steepened over time to reach its present vertical geometry, as proposed for other strike-slip faults that initially reactivated preexisting dipping structures (e.g. Mason et al., 2017; Dorsey et al., 2012).

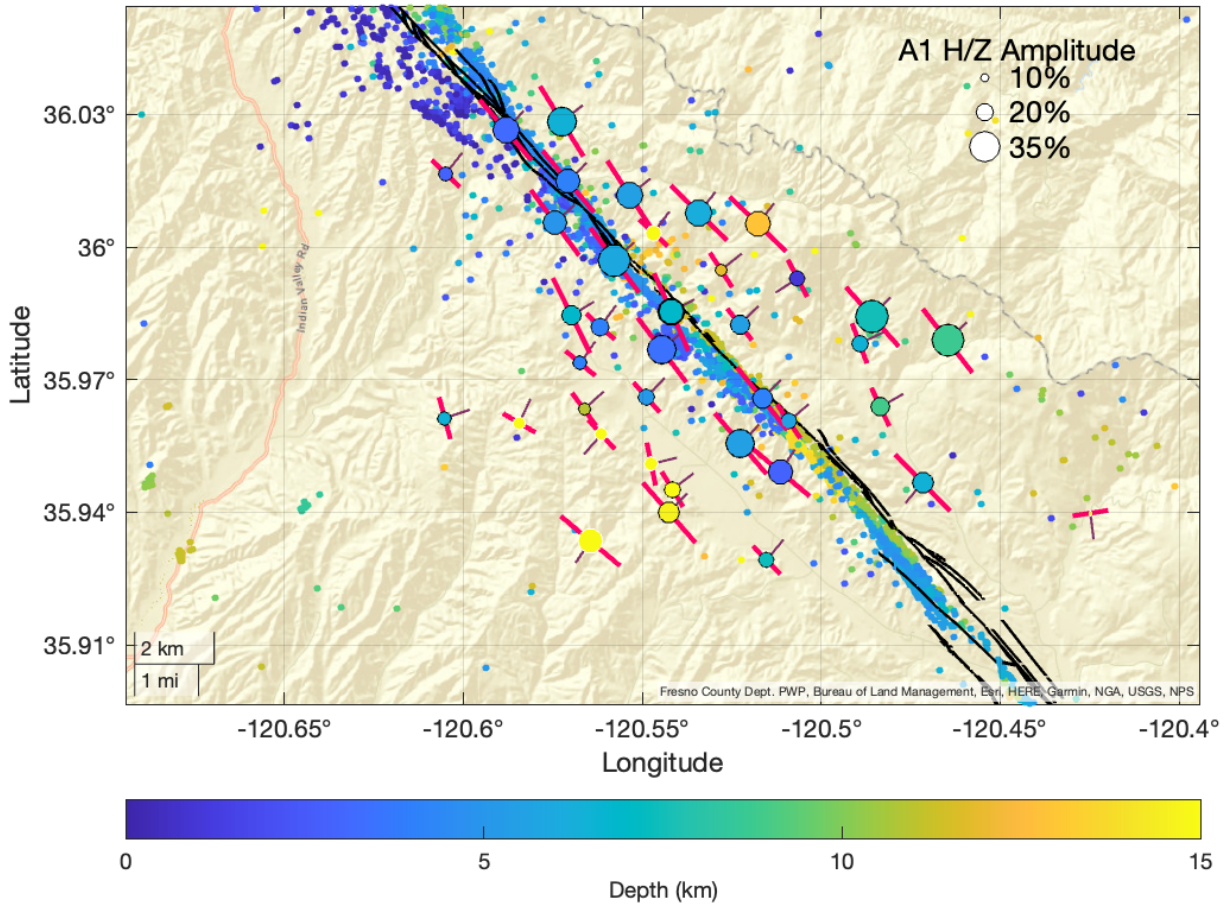

Fig. 1: Seismicity and receiver function results across the San Andreas Fault near Parkfield. Background shows topographic shading. Small dots without an outline are seismicity from the GrowClust double difference catalog, colored by depth. Black lines are surface fault traces from the USGS fault database (the current CFM ends in the center of the map region). Circles are receiver function results displayed at the location of each station. The circle size shows the amplitude of the largest degree-1 (360º periodicity; A1) azimuthal harmonic arrival at each station, colored by the depth of the contrast in anisotropy on the same color scale as seismicity. Red bars show the foliation strike of the stronger anisotropic fabric across the contrast. Black tickmarks show the phase of the A1 arrival; they point downdip if assuming the foliation is stronger below the contrast that generates the conversion.

Comparison to Mojave, San Jacinto fault zone, and regional results

We analyzed data from a temporary deployment in the Mojave that crosses several minor strike-slip faults to obtain a comparison to the more mature San Andreas fault. Results are shown in Fig. 3. Strikes show more scatter than those in Parkfield, although some near-fault stations show strikes parallel to the fault, and strikes are peaked near the regional fault trend around NW. The Mojave observed A1 amplitudes are much smaller than those at Parkfield.

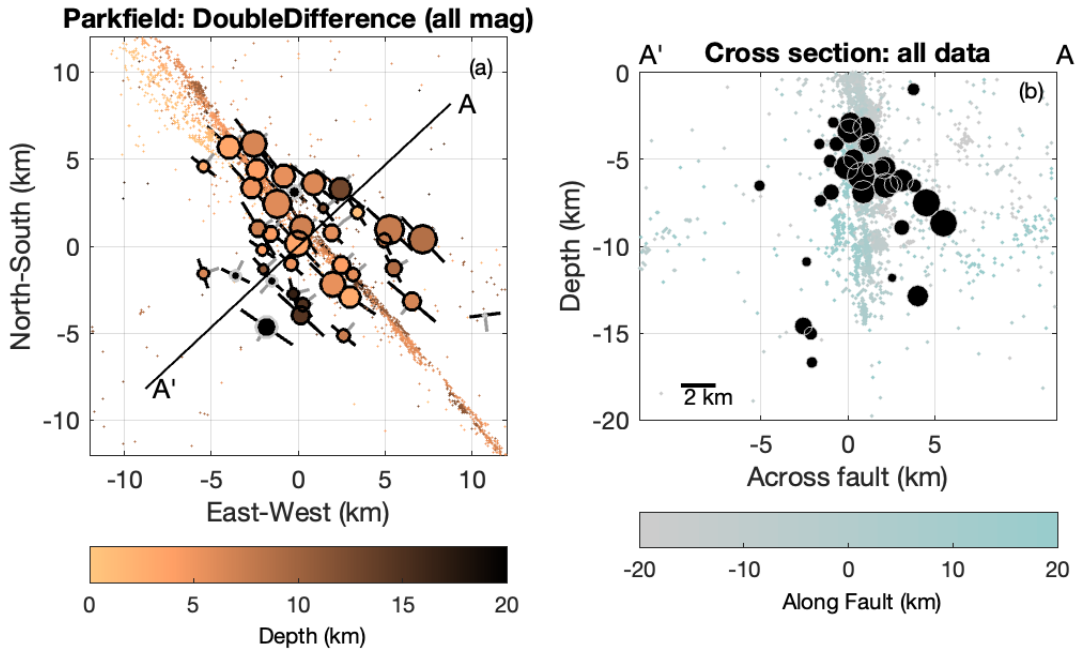

Fig. 2: San Andreas fault near Parkfield, California. (left) Seismicity as dots, colored by hypocenter depth. Circles with bars represent the largest first azimuthal harmonic receiver function conversion at each station, plotted at the station location; circles are scaled by conversion amplitude and colored by depth. Black two-sided bars show the foliation strike. Grey short bars show downdip direction, assuming anisotropy is stronger below the converting contrast; note consistent NE dip on both sides of the surface fault trace. (right) Cross-sectional view of seismicity colored by along-fault distance; black dots are receiver function anisotropic conversions, sizes scaled by amplitude.

In a regional comparison, the San Andreas and Mojave examples shown above fall on opposite ends of the range of amplitudes seen in receiver function A1 conversion amplitudes. Fig. 4 shows results from a fault-crossing network in the San Jacinto fault zone trifurcation area, with fault-parallel features seen in A1 arrival strikes as well as seismicity. Results for all three areas in context with the regional average for southern California (Schulte-Pelkum et al., 2020) are shown in Fig. 5. The results support a **trend of increasing A1 amplitudes with fault maturity**, with the San Andreas fault near Parkfield showing the strongest A1 conversions, followed by the San Jacinto fault zone, then the regional average, and the smallest amplitudes seen from the dense station line crossing minor strike-slip faults in the Mojave.

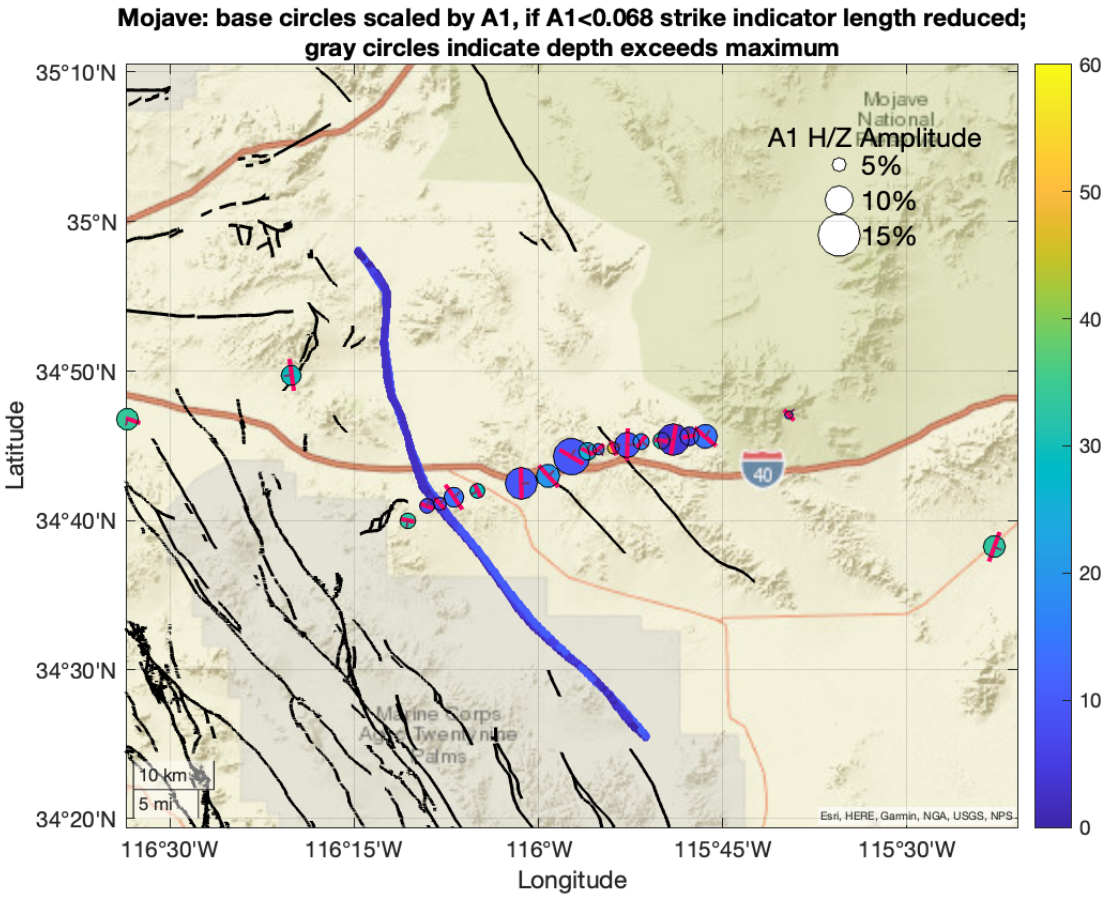

Fig. 3: Receiver function results from a fault-crossing temporary dense line deployment in the Mojave. Background shows topographic shading and major roads. Black lines are surface fault traces from the USGS fault database. Blue line is CFM representation of the Ludlow fault (the only fault in this region represented in the CFM), with dots on the fault surface colored by depth in km. Receiver function results as in Fig. 1 (note the difference in amplitude scale).

SUMMARY AND CONCLUSIONS

This work used azimuthal harmonic arrivals to image the depth, amplitude, and strike of conversions from contrasts in dipping foliation and dipping contrasts between isotropic bodies, an approach particularly well suited to mapping shear zones, dipping faults, and tectonic boundaries (Schulte-Pelkum et al., 2014a,b, 2020a,b). We compared these receiver function strike orientations and depths with those from the SCEC CFM5.3 and relocated seismicity catalogs (QTM and GrowClust). We find general parallelism of receiver function-derived crustal fabric strikes with strikes of nearby faults in the CFM5.3 and planar features delineated in the relocated seismicity. We find increased alignment of receiver function strikes with fault strikes as well as increasing receiver function A1 amplitudes with fault maturity. Additionally, we find indications for interactions between inherited fabric and present-day faulting and deformation.

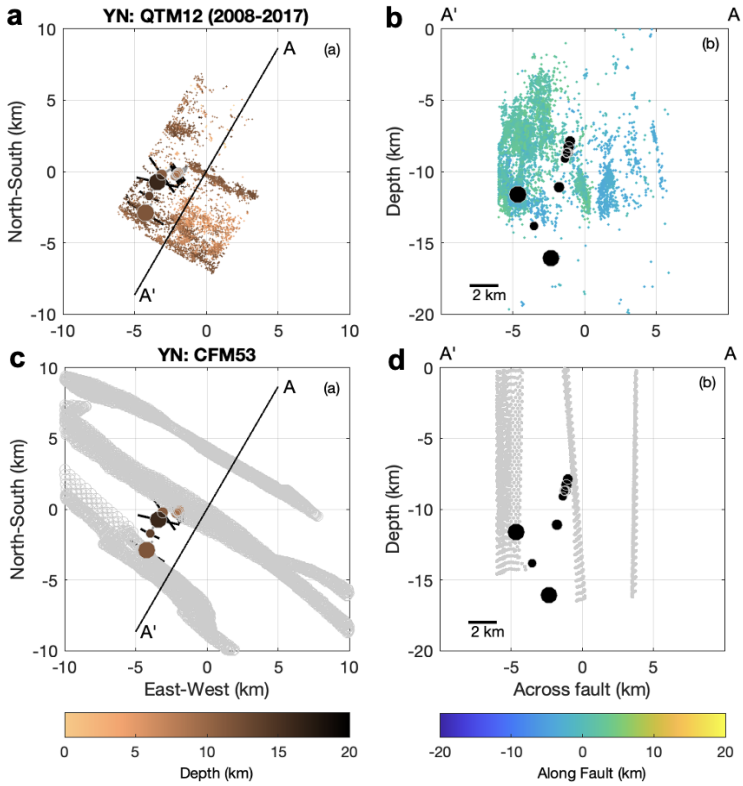

Fig. 4: Results from a dense line of broadband stations crossing the San Jacinto fault zone in the trifurcation area (Vernon, 2010; Qiu et al., 2017). (a) Seismicity (dots) from the catalog by Ross et al. (2019) and A1 arrivals (circles), both colored by depth. Black bars are A1 phase, interpreted as foliation strike. (b) Same seismicity (dots) and A1 conversions (black circles, scaled by amplitude) on A'-A cross section. (c) A1 arrivals (same as in a) and CFM fault shapes (grey). (d) Fault shapes and A1 arrivals on A'-A cross section.

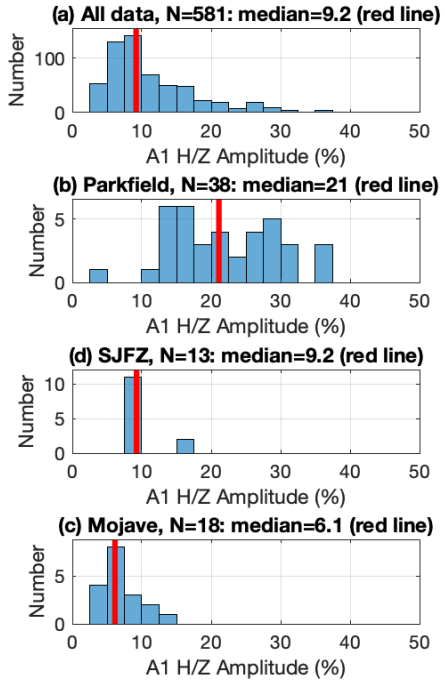

Fig. 5: Histograms of the largest receiver function A1 amplitude per station in different subsets. (a) All data, including all stations across southern California published in Schulte-Pelkum et al. (2020). The vertical axis shows the station count, and the horizontal axis shows the amplitude of the largest A1 arrival at each station as a fraction of the horizontal to vertical arrival amplitude. The red line shows the median value. (b) As in a, but for Parkfield stations shown in Fig. 1. (c) Results from a dense fault-crossing station line in the San Jacinto fault zone. (d) Mojave station subset shown in Fig. 3.

References Cited

Brownlee, S. J., V. Schulte-Pelkum, A. Raju, K. Mahan, C. Condit, and O. F. Orlandini (2017), Characteristics of deep crustal seismic anisotropy from a compilation of rock elasticity tensors and their expression in receiver functions, Tectonics, 36, doi:10.1002/ 2017TC004625.

Dorsey, R. J., G. J. Axen, T. C. Peryam, and M. E. Kairouz (2012), Initiation of the Southern Elsinore Fault at $1.2 Ma: Evidence from the Fish Creek–Vallecito Basin, southern California, Tectonics, 31, TC2006, doi:10.1029/2011TC003009.

Hauksson, E., W. Yang, and P. M. Shearer, Waveform Relocated Earthquake Catalog for Southern California (1981 to June 2011), *Bulletin of the Seismological Society of America*, *102*(5), 2239–2244, doi:10.1785/0120120010, 2012.

Hearn, L., S. Marshall, and L. Montesi, Highlights of SCEC Community Modeling Efforts and a Vision for Community Models in the Next Earthquake Center, 2020.

Hughes, A., R. Bell, Z. Mildon, D. Rood, A. Whittaker, T. Rockwell, Y. Levy, D. DeVecchio, S. Marshall, and C. Nicholson, Three-dimensional structure, ground rupture hazards, and static stress models for complex nonplanar thrust faults in the Ventura basin, southern California, *Journal of Geophysical Research: Solid Earth*, *125*(7), e2020JB019,539, 2020.

Maechling, P., M. Su, E. Hearn, S. Marshall, A. Plesch, S. J.H., O. M.E., M. L.G., P. E., H. T.T., and B. Y., Developing Web-based Visualization and Query Tools for the SCEC CVM, CFM, GFM, and CTM Community Models, *Poster Presentation at 2020 SCEC Annual Meeting*, 2020.

Mason, C. C., Spotila, J. A., Axen, G., Dorsey, R. J., Luther, A., & Stockli, D. F. (2017). Two-phase exhumation of the Santa Rosa Mountains: Low- and high-angle normal faulting during initiation and evolution of the southern San Andreas Fault system. Tectonics, 36, 2863–2881. https://doi.org/10.1002/ 2017TC004498.

Nicholson, C., A. Plesch, C. Sorlien, J. H. Shaw, and E. Hauksson, Updates, Evaluation and Improvements to the Community Fault Model (CFM version 5.3), *Poster Presentation at 2020 SCEC Annual Meeting*, 2020.

Plesch, A., S. Marshall, C. Nicholson, P. J. Maechling, and M. Sue, The Community Fault Model version 5.3 and new web-based tools., *Poster Presentation at 2020 SCEC Annual Meeting*, 2020a.

Plesch, A., J. H. Shaw, Z. E. Ross, and E. Hauksson, Detailed 3D Fault Representations for the 2019 Ridgecrest, California, Earthquake Sequence, *Bulletin of the Seismological Society of America*, *110*(4), 1818–1831, 2020b.

Qiu, H., Ben-Zion, Y., Ross, Z. E., Share, P. E., & Vernon, F. L. (2017). Internal structure of the San Jacinto fault zone at Jackass Flat from data recorded by a dense linear array. Geophysical Journal International, 209(3), 1369-1388.

Ross, Z. E., D. T. Trugman, E. Hauksson, and P. M. Shearer, Searching for hidden earthquakes in Southern California, *Science*, *364*(6442), 767+, doi:10.1126/science.aaw6888, 2019.

Ross, Z. E., Idini, B., Jia, Z., Stephenson, O. L., Zhong, M., Wang, X., ... & Jung, J. (2019). Hierarchical interlocked orthogonal faulting in the 2019 Ridgecrest earthquake sequence. *Science*, *366*(6463), 346-351.

Schulte-Pelkum, V., and K. H. Mahan, A method for mapping crustal deformation and anisotropy with receiver functions and first results from USArray, *Earth Planet. Sci. Lett.*, *402*(SI), 221–233, doi:10.1016/j.epsl.2014.01.050, 2014a.

Schulte-Pelkum, V., and K. H. Mahan, Imaging Faults and Shear Zones Using Receiver Functions, *Pure Appl. Geophys.*, *171*, 2967–2991, doi:10.1007/s00024-014-0853-4, 2014b.

Schulte-Pelkum, V., Z. Ross, K. Mueller, and Y. Ben-Zion, Tectonic inheritance with dipping faults and deformation fabric in the brittle and ductile southern California crust, *J. Geophys. Res.*, *125*(8), e2020JB019,525, doi:10.1029/2020JB019525, 2020b.

Thurber, C., S. Roecker, K. Roberts, M. Gold, L. Powell, and K. Rittger, Earthquake locations and three-dimensional fault zone structure along the creeping section of the San Andreas Fault near Parkfield, CA: preparing for SAFOD, *Geophys. Res. Lett.*, *30*, doi:doi:10.1029/2002GL016004, 2003.

Thurber, C., S. Roecker, H. Zhang, S. Baher, and W. Ellsworth, Fine-scale structure of the San Andreas fault and location of the SAFOD target earthquakes, *Geophys. Res. Lett.*, *31*, L12S02, doi:doi:10.1029/2003GL019398, 2004.

Trugman, D. T., & Shearer, P. M. GrowClust: A hierarchical clustering algorithm for relative earthquake relocation, with application to the Spanish Springs and Sheldon, Nevada, earthquake sequences. *Seismological Research Letters*, 379-391, 2017.

Vernon, F. & Yehuda Ben-Zion. San Jacinto Fault Zone Experiment. International Federation of Digital Seismograph Networks. https://doi.org/10.7914/SN/YN_2010, 2010.